Chapter 10
Optical Fibre Probe with Lateral Interface

Makoto Tsubokawa

Abstract This paper proposes a novel optical fibre probe containing a scattering layer that is capable of sensing the surrounding light through the lateral surface of the fibre. The performance of the probe in sensing various target objects in free space and water environment has been evaluated by ray-trace simulation. For the probe of diameter 1 mm and length 50 mm, the normalised power, which is defined as the ratio of the signal power to the source power, was obtained within 0.1–0.01 % for the target object over a surrounding space with a radius of ~20 mm. Besides, the probe exhibits sharp directional property with an angular diameter of ~10° in the radial direction. Utilizing this functionality, the probe with the spiral-shaped scattering part will enable the sensing of target objects that are spatially distributed along a fibre axis with a minimum detectable gap of less than 2 mm.

10.1 Introduction

Because of their thin structure and ease of fabrication, there have been many studies on light concentrators with acceptance top/side surfaces of planar waveguides/optical fibres. Most of them are relevant to the well-known luminescent solar concentrator [5, 9, 15]; in contrast, simple concentrator that directly collect illumination light have not been fully explored because of their low efficiency [6, 14]. However, this simple scheme appears to be attractive for optical sensor applications because it may produce versatile applications by expanding the optical interface from a point to the surface. As an interesting example, the integration of optical fibres into textile structures called photonic textiles has been proposed to realize multifunctional sensors such as wearable photodetectors (PDs) or direction sensors of light beams [1, 3, 11]. We are currently studying this technique to enable

M. Tsubokawa (✉)
Waseda University, Kitakyusyu, Japan
e-mail: tsubokawa.m@waseda.jp

P.A. Ribeiro and M. Raposo (eds.), *Photoptics 2014*,
Springer Proceedings in Physics 177, DOI 10.1007/978-3-319-27321-1_10

their application as thin optical probes used to sense the surroundings. In general, such optical probes need to incorporate micro-lens systems or several optical fibres, and should sweep over the target space because a point detector only gets a point image [2, 4, 8, 10, 12, 16]. If the detection through the side-surface interface is applicable, it may not only simplify the sweep mechanism but also enable us to realize passive optical probes without the need for precise lens systems.

In this study, we show a new design of thin fibre-optic probe with a side surface interface, and evaluate basic characteristics by performing ray-trace simulations [7]. Both light source (LS) for illuminating target objects and a PD are attached to the end of an optical fibre, and the light propagation through a side surface is adjusted by a Mie scattering layer embedded in the optical fibre. We show the output signal of the probe as a function of the size, position and materials comprising the target object, and finally evaluate the spatial distribution of the target and its resolution.

10.2 Fibre-Optic Probe Model

Figure 10.1 shows the probe model consisting of two serially concatenated guides and sensor parts. The parameters used in our simulation for the waveguide and light source are listed in Table 10.1. The guide part has a two-layered structure with an outer coating as an absorber in which the core guiding input light from a light source is embedded in the bottom of the cladding in addition to a normal core. A light source and PD are attached to the end face of each core. The sensor part has the scattering part at the bottom in the cladding, which is connected to the bottom core in the guide part. Light scattering is observed in the scattering part (width D) composed of a cluster of air particles with a particle number density ρ. The width D is defined as the arc length corresponding to the width of the focus zone for normal incident light and is calculated using the size and refractive indices of the optical fibre. The minimal arrangement of the scattering part effectively generates light components in the direction of the target and suppresses excess loss during propagation along the fibre. Because of reducing D, the high index fibre is used in the simulation. Input lights are scattered in the sensor part and a portion of them reaches the target object owing to the lens effect in cylindrical optical fibre. Lights reflected at the target partially re-enter the optical fibre, and are either scattered again and transmitted to the PD or are escaped to the outside. As shown in Fig. 10.1, we assume the square target object of $w_1 \times 2w_2 \times \delta w$ at distances d_1 and d_2 above the sensor part. Angles ψ is the angular diameter of the target. For simplicity, we assume the bottom surface of the target plane is a 96 % reflector as a reference. Here we define the normalised received power η_{probe} as the ratio of light power that reaches the PD's surface by way of the target plane to the light power of the source. In our model, η_{probe} estimated by the ray-trace simulation gives results that are equivalent to the case using incoherent light without interference effects. Under the Mie scattering model used in this simulation, the wavelength dependence

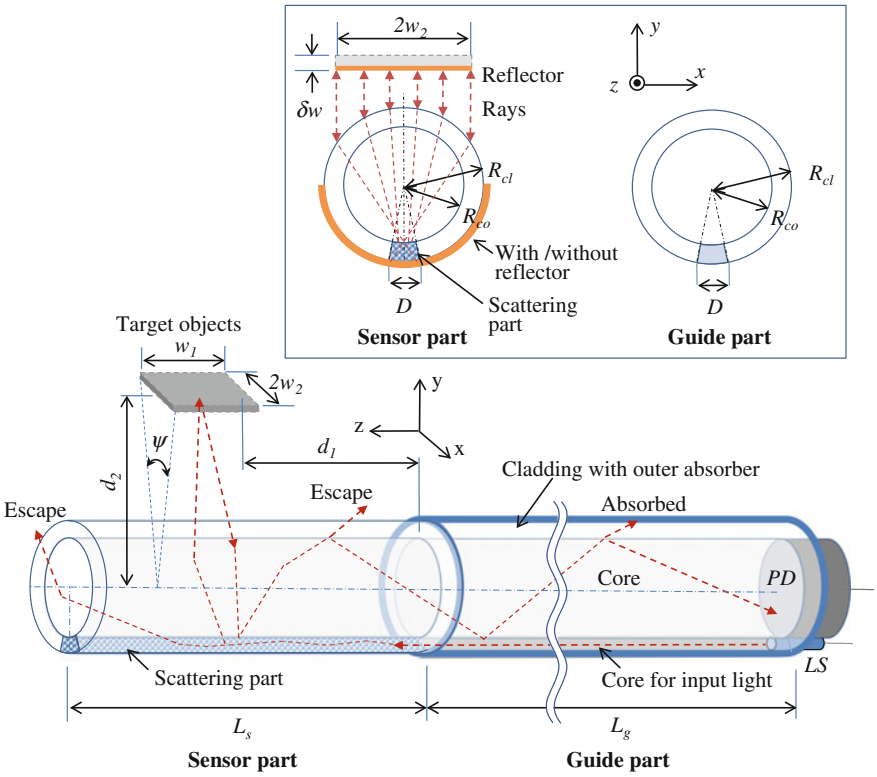

Fig. 10.1 Fibre-optic probe model

Table 10.1 Parameters of fibre-optic probe

Optical fibre	Sensor part	Guide part
Core radius R_{co}	0.5 mm	0.5 mm
Cladding radius R_{cl}	0.55 mm	0.55 mm
Refractive index of core	1.83	1.83
Refractive index of core for input light	1.86	1.86
Refractive index of cladding	1.86	1.46
Particle radius r (material)	250 nm (air)	None
Particle number density ρ	2.3×10^8 mm^{-3}	None
Width of scattering part D (Central angle)	0.07 mm (7.5°), 0.3 mm (31°)	
Length L_s, L_g	50 mm	50 mm
Light source and photodetector		
Wavelength	550 nm	
Polarisation	Random	
Source position	Embedded in end of core for input light	
Photodetector	Area detector attached on core end face	

Refractive indices of 1.86 (LaSFN9), 1.83 (LaSFN40), 1.46 (SiO_2) are assumed [13]

is almost negligible over a broadband spectrum such as natural light; therefore, we use a monochromatic source of 550 nm wavelength with a random polarisation instead of a broadband light source.

10.3 Simulation Results

10.3.1 Normalised Received Power η_{probe}

Figure 10.2 shows η_{probe}, which is dependent on the distance d_2 and width w_2. Here $d_1 = 0$ and $w_1 = L_s = 50$ mm. The particle number density ρ is assumed to be 2.3×10^8 mm^{-3} because η_{probe} has a maximum for this model in our simulation. Larger ρ causes not only larger scattering efficiency but also excess loss in light propagation along a fibre. Under this condition, 22 and 36 % of the source power arrive at the target plane through the sensor part with and without the 96 % reflector, respectively. Although these are due to scattering and lens effect in a fibre, it is fairly high efficiency without imaging optics. We can see in Fig. 10.2 that η_{probe} does not vary much for $d_2 \leq 2$ mm, but above 2 mm, it tends to decrease. If the incident angle distribution to the target object is uniform, the number of round-trip rays between the sensor part and the target is roughly proportional to a half of the angular diameter $\psi(d_2)/2$, and then $\eta_{probe} \propto \psi(d_2)/2 = 2\tan^{-1}[w_2/2d_2]$. In fact,

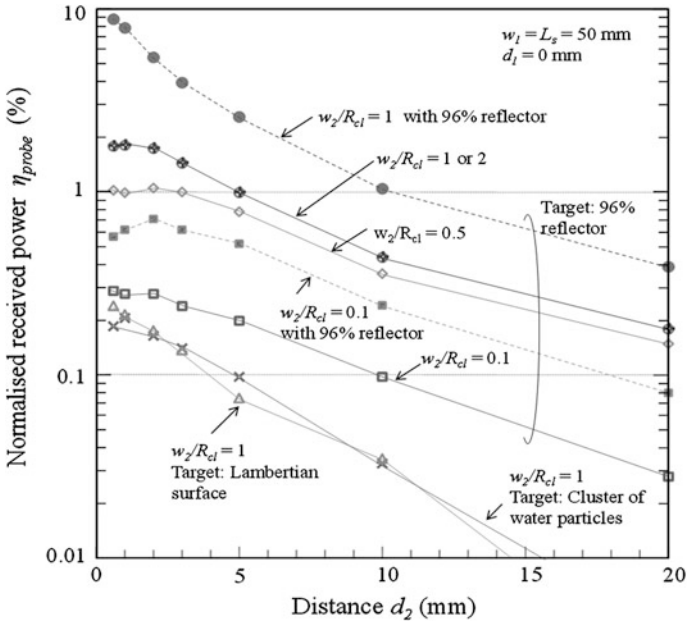

Fig. 10.2 Normalised received power η_{probe} as a function of distance d_2 and width w_2/R_{cl}

the downward curves in Fig. 10.2 indicate the presence of a slightly small slope compared to the variation of $\psi(d_2)/2$ because light components with nearly normal incidence dominate owing to the lens effect in optical fibre. On the other hand, η_{probe} decreases at a rate smaller than w_2/R_{cl} because light components other than normal incidence can re-enter the sensor part when $w_2/R_{cl} < 1$. Regarding the received power, for example, η_{probe} is approximately 0.3 and 1.8 % for $w_2/R_{cl} = 0.1$ and 1, respectively, at $d_2 = 2$ mm, when the sensor part has no reflector. These values are much smaller than the rate of light power that reaches the target plane as mentioned above, which suggests that the optical loss after reflection at the target plane is significant in our model. Actually, 3–4 dB loss is observed only at the boundary between the sensor and guide parts, which remains an issue. When the 96 % reflector is attached to the sensor part, η_{probe} was more than doubled, i.e. 0.7 and 5 % for $w_2/R_{cl} = 0.1$ and 1, respectively, at $d_2 = 2$ mm. In Fig. 10.2, we also plot curves for different type of targets—the Lambertian reflector and cluster of water particles as a Mie scattering object ($\delta w = 0.5$ mm, $r = 250$-nm). They indicate that η_{probe} is smaller and more steeply decrease as compared to the case of a simple target with a reflector. These are seen as the results from the spread of the reflection angle and lower reflectivity at the target object.

Next, the dependence of η_{probe} on the target length w_1 and position d_1 along a fibre axis is shown in Fig. 10.3. Another scale of the power ratio of $(\eta_{probe}-\eta_{bias})/\eta_{probe}$ has also been plotted, where η_{bias} is defined as the ratio of light power that reaches the PD's surface in the absence of the target object to the light power of the source. We can see that η_{probe} is nearly proportional to w_1 and it exponentially decreases with

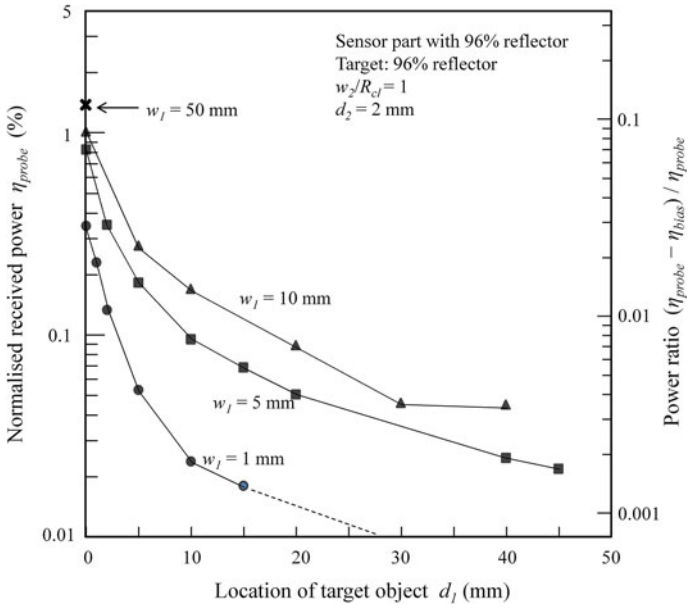

Fig. 10.3 Normalised received power η_{probe} as a function of location d_1 and length w_1

an increase in d_1. This is because the spread of the incidence angle in the y–z plane has a similar influence on targets of different w_1, and an increase in d_1 remarkably reduces the transmission loss along the sensor part. From these results, we can estimate the location when the target size is given, and vice versa. In fact, if we need to simultaneously sense both size and location without a sweep operation, an additional scheme is required. We discuss this issue in the next section. As shown in Fig. 10.3, the power ratio of $(\eta_{probe}-\eta_{bias})/\eta_{probe}$ is relatively small (0.1–0.01). Although it is similar to the signal to noise ratio, the signal component of the η_{probe} can be obtained by determining the separation from η_{bias}, as it is almost constant regardless of the target. Enhancing $(\eta_{probe}-\eta_{bias})/\eta_{probe}$ becomes one of the important issues in suppressing the influence of the shot noise during the actual experiments.

10.3.2 Evaluation Under Water Environment

Next, we consider a case involving the use of our model in water, e.g. probe biological cells in the body. Because the refraction angle becomes small under water conditions, we designed another probe structure with width D calculated to be 0.3 mm according to the definition. Figure 10.4a, b show the η_{probe} as a function of distance d_2 under the water condition. Here target objects of 1.1 × 50 mm are (a) 96 % reflector and (b) examples of Mie models and biological objects with δw = 1 mm.

We see in Fig. 10.4a that η_{probe} is obviously improved at D = 0.3 mm compared to D = 0.07 mm in the short d_2 region for the case with/without reflector on the sensor part. For a distance of $d_2 > 5$ mm, the advantage decreases when using the sensor part without the reflector. This is because the number of round-trip rays between the fibre and the target is enhanced by the scattering part with an optimum D (= 0.3 mm). However, the propagation loss owing to the excess scattering along a fibre also tends to increase with increase in d_1. This loss effect is mitigated by positioning a reflector on the sensor part. In Fig. 10.4b, we see that the skin dermis shows a higher reflectivity compared to the epidermis and Mie model of air particles (LightTools, Synopsys, Inc.). These results mainly indicate the differences of the reflectivity of the objects, which are useful when discerning target objects.

10.3.3 Evaluation of Spatially Distributed Targets

When an optical needle probe with a point detector is applied to sense a 3D space, it usually needs to be swept over the target plane; moreover, the time/frequency domain immersion or optical coherence tomography (OCT) techniques are usually applied to resolve the depth information. Here we focus on the approach that is used to simplify the sweep operation and set aside the techniques of immersion or OCT. Because our method can extract the information of an object arranged linearly along

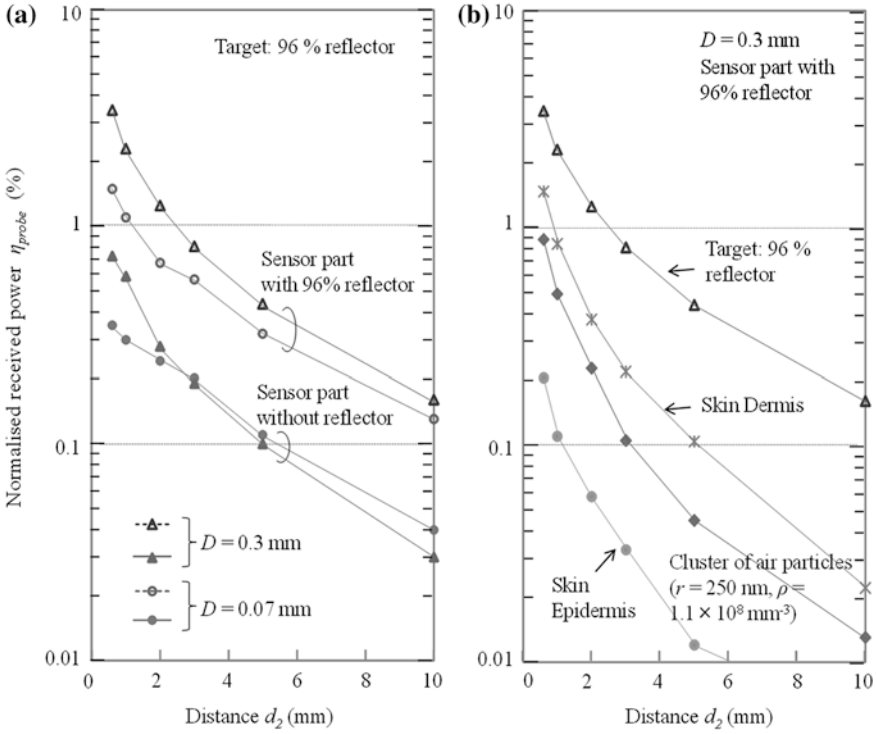

Fig. 10.4 Normalised received power η_{probe} as a function of d_2 under water conditions. The thickness δw of skin dermis, epidermis and cluster of air particles are 1 mm

the probe, the linear distribution of an object may be detected without a complex sweep operation. Figure 10.5 shows the sensor part, which has a spiral-shaped scattering part embedded in cladding. This is the same structure as the 360° twisted sensor part in Fig. 10.1.

Initially, we analysed the directional property of the simple fibre-optic probe with straight scattering part, shown in Fig. 10.1. Figure 10.6 shows the radar chart of η_{probe} plotted as a function of θ_{fibre}, the angle at which the probe is rotated with respect to the reflector. The measurements were performed assuming 96 % mirror target of 50 × 1.1 mm, d_2 = 2 mm and D = 0.07 mm. As can be easily predicted from the geometric structure of the sensor part, η_{probe} indicates the distinct directional property of the target in the direction opposite to the scattering part (180°). The full width at half maximum of the peak is ∼10°. This result implies that the probe is capable of observing the surrounding light distribution as a function of the incident angle in the x–y plane.

Next, supposing the twisted sensor part, the sensor is capable of sensing the target plane that is continuously twisted at an angle θ_{TP}, as shown in Fig. 10.5. This could be ascribed to the sharp directional property of the sensor, as mentioned above. Here, $\theta_{TP} = 360d_1/L_s°$. From a different viewpoint, we can detect the

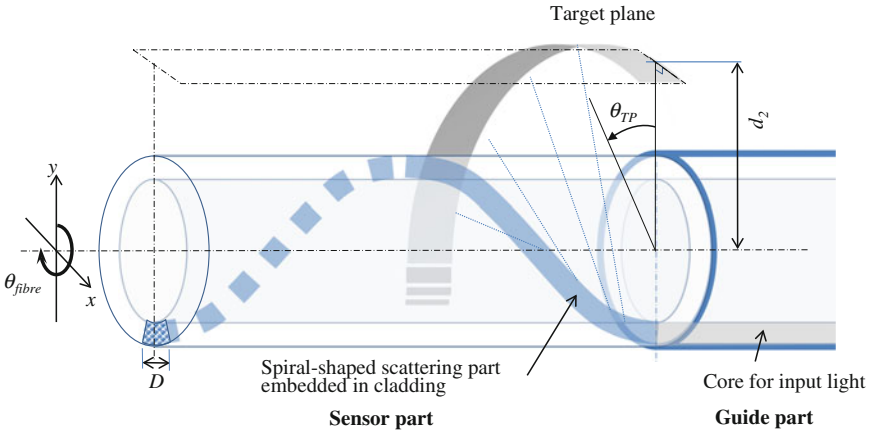

Fig. 10.5 Fibre-optic probe with spiral-shaped scattering part

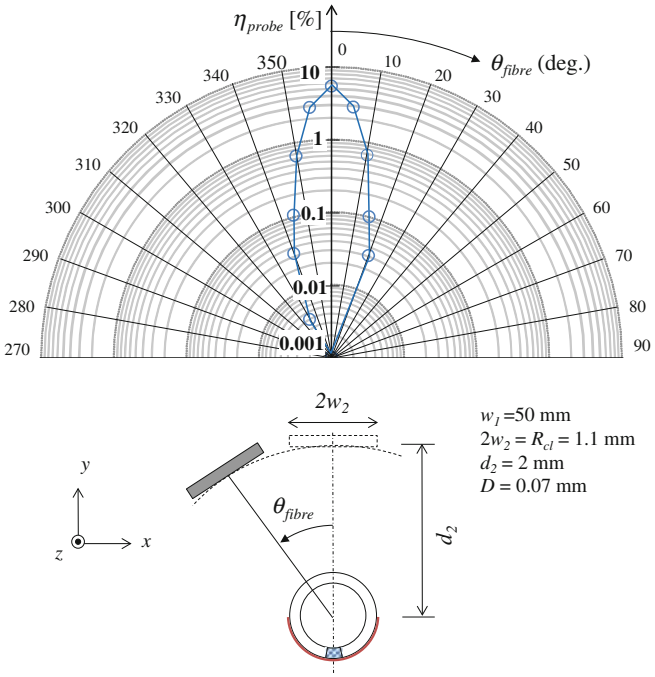

Fig. 10.6 Radar chart of normalised received power η_{probe} in straight sensor part

distribution of the target plane positioned above the sensor part (parallelogram of dash-dotted line) when the optical fibre is rotated by $0° \leq \theta_{fibre} < 360°$, where $\theta_{fibre} = -\theta_{TP}$. Figure 10.7 shows the normalised received power η_{probe} as a function of θ_{fibre}. The reflector is similarly twised with the scattering part on the sensor

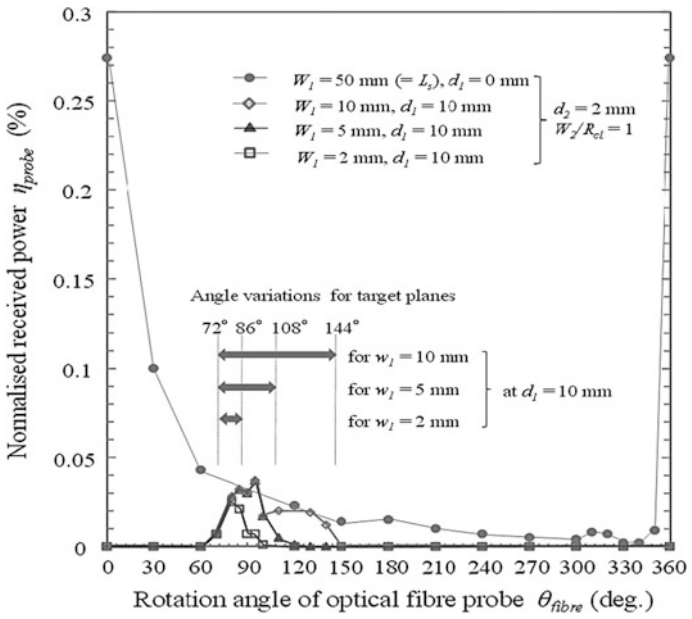

Fig. 10.7 Normalised received power η_{probe} in the twisted sensor part as a function of the angle of rotation θ_{fibre}

part. The curve with filled circles indicates η_{probe} for the target of w_1 = 50 mm, w_2/R_{cl} = 1, d_1 = 0 mm and d_2 = 2 mm, which corresponds to the maximum η_{probe} at θ_{fibre}. The curve shows a steep decline with an increase in θ_{fibre} because of the constant value of ρ along the fibre axis. This tendency is similar to the results for $1 < w_1 < 5$ mm, shown in Fig. 10.3. The peak width of ~26° at θ_{fibre} = 0° is broader than that shown in Fig. 10.6, as the centre of the lightning area on the target exhibits a certain angular spreading along the z-axis due to the spiral form of the scattering part. Three curves obtained for targets of w_1 = 2, 5 or 10 mm at d_1 = 10 mm are also shown in Fig. 10.7, and the angles of peak locations and widths of three peaks are roughly estimated to be 80°, 90° and 110° and 15°, 28° and 60°, respectively. On the other hand, the four angles of edge locations in the target are calculated to be 72°, 86°, 108° and 144°, as shown in Fig. 10.7. As is seen, the peak locations are in good agreement with each other, and that the peak width well reflects the target length w_1. As the three curves are segments of the maximum curve (filled circle symbols), the peak position and width corresponding to larger w_1 tend to be fuzzy. Nevertheless, they are relatively precise for $w_1 \leq 5$ mm.

Finally, we evaluate two targets arranged in tandem with a small gap δd to check the spatial resolution. From Fig. 10.7, the angle resolution of ~15° is predicted for two targets of length 2 mm. Figure 10.8 shows η_{probe} for two targets with δd = 2 and 1 mm, respectively. Here, w_1 = 2 mm and w_2/R_{cl} = 1. Two peaks in the curve for δd = 2 mm are clearly observed, and the peak interval is estimated to be 4.2 mm for

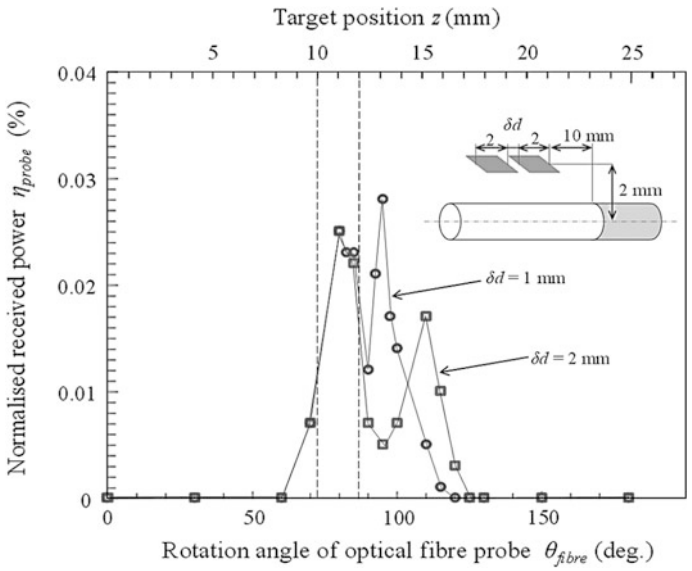

Fig. 10.8 Curves of normalised received power η_{probe} for the targets with a small gap. Two target planes where $w_1 = 2$ mm, $w_2/R_{cl} = 1$, $d_1 = 10$ mm and $d_2 = 2$ mm are arranged in tandem with a gap δd of 1 and 2 mm

an angle difference of 30°. Because the peak location indicates the centre of the target, the peak interval is approximately given by $\delta d + w_1$ and δd is almost the same as real gap of 2 mm. For the case of $\delta d = 1$ mm, we also find two peaks with an interval of 15°, corresponding to 2.1 mm, which is slightly smaller than the expected value of 3 mm ($= \delta d + w_1$), and is caused by the peak shift effect due to the overlapping of different height pulses. Consequently, under this condition, the spatial resolution for the gap is estimated to be slightly less than 2 mm.

10.4 Conclusions

We proposed a simple fibre-optic probe with a side-surface interface against a target space, and evaluated the basic performance by performing ray-trace simulations. Our model has a needle shape of approximately 1-mm diameter and 50-mm length, which enables us to detect the normalised light power of 0.01–10 % of the source power when target objects are located in a surrounding cylinder space with an $\sim$20-mm radius. Under water conditions, the sensitivity was easily improved by adjusting the size of the scattering part. Moreover, by using the directional property of the probe twisted by 360°, the targets distributed along the fibre axis with a minimum detectable gap of less than 2 mm could be measured.

In our future work, we firstly aim to improve the signal level by optimizing the probe structure and materials, for example, the shape of the fibre and particle number density distribution of the scattering parts may bring about desirable effects such as narrow focus area and smooth sensitivity along a fibre. As next step aim, we need to incorporate a key technique such as the OCT technique for our method to resolve radially distributed targets.

Acknowledgements Part of the research presented in this paper has been done under JSPS KAKENHI Grant Number 25420346.

References

1. A.F. Abouraddy, Towards multifunctional fibres that see, hear, sense and communicate. Nat. Mater. **6**, 336–347 (2007)
2. R.R. Ansari, Microemulsion characterization by the use of a noninvasive backscatter fibre optic probe. Appl. Opt. **32**, 3822–3827 (1993)
3. G. Cho (ed.), in *Smart clothing technology and applications*. (CRC Press, 2010), pp. 115–134
4. J.S. Dam, Fibre-optic probe for noninvasive real-time determination of tissue optical properties at multiple wavelengths. Appl. Opt. **40**, 1155–1164 (2001)
5. O. Edelenbosch, Luminescent solar concentrators with fibre geometry', OSA Opt. Express **21**, 503–513 (2013)
6. J.M. Kim, Optical efficiency-concentration ratio trade-off for a flat panel photovoltaic system with diffuser type concentrator. Sol. Energy Mater. Sol. Cells **103**, 35–40 (2012)
7. LightTools, Synopsys Inc. http://www.opticalres.com. Accessed 20 May 2013
8. D. Lorenser, Ultrathin side-viewing needle probe for optical coherence tomography. Opt. Lett. **36**, 3894–3896 (2011)
9. K.R. Mcintosh, Theoretical comparison of cylindrical and square-planar luminescent solar concentrators. Appl. Phys. B **88**, 285–290 (2007)
10. D. Piao, Endoscopic, rapid near-infrared optical tomography. Opt. Lett. **31**, 2876–2878 (2006)
11. M. Rothmaier, Photonic textiles for pulse oximetry. Opt. Express **16**, 12973–12986 (2008)
12. D.D. Sampson, Microscope-in-a-needle technology for deep-tissue 3D imaging, in *Proceedings of the International Conference on Information Photonics*, pp. 1–2
13. Schott Glass Inc. http://www.schott.com/advanced_optics/us/abbe_datasheets/schott_datasheet_all_us.pdf. Accessed 20 Dec 2014
14. M. Tsubokawa, A novel Fibre-optic concentrator with scattering pars. IEICE Trans. Electron. E97-C:93–100 (2014)
15. W.G.J.H.M. Van Sark, Luminescent solar concentrators—a review of recent results. Opt. Express **16**, 21773–21792 (2008)
16. Q. Wang, Measurement of internal tissue optical properties at ultraviolet and visible wavelengths: Development and implementation of a fibreoptic-based system. Opt. Express **16**, 8685–8703 (2008)